

Concurrently Approaching Volumetric and Specific Capacity Limits of Lithium Battery Cathodes via Conformal Pickering Emulsion Graphene Coatings

Kyu-Young Park, Jin-Myoung Lim, Norman S. Luu, Julia R. Downing, Shay G. Wallace, Lindsay E. Chaney, Hocheon Yoo, Woo Jin Hyun, Hyeong-U Kim, and Mark C. Hersam*

To achieve the high energy densities demanded by emerging technologies, lithium battery electrodes need to approach the volumetric and specific capacity limits of their electrochemically active constituents, which requires minimization of the inactive components of the electrode. However, a reduction in the percentage of inactive conductive additives limits charge transport within the battery electrode, which results in compromised electrochemical performance. Here, an electrode design that achieves efficient electron and lithium-ion transport kinetics at exceptionally low conductive additive levels and industrially relevant active material areal loadings is introduced. Using a scalable Pickering emulsion approach, Ni-rich $\text{LiNi}_{0.8}\text{Co}_{0.15}\text{Al}_{0.05}\text{O}_2$ (NCA) cathode powders are conformally coated using only 0.5 wt% of solution-processed graphene, resulting in an electrical conductivity that is comparable to 5 wt% carbon black. Moreover, the conformal graphene coating mitigates degradation at the cathode surface, thus providing improved electrochemical cycle life. The morphology of the electrodes also facilitates rapid lithium-ion transport kinetics, which provides superlative rate capability. Overall, this electrode design concurrently approaches theoretical volumetric and specific capacity limits without tradeoffs in cycle life, rate capability, or active material areal loading.

1. Introduction

As confirmed by the 2019 Nobel Prize in chemistry, lithium-ion batteries (LIBs) have become ubiquitous with a profound impact on diverse technologies including portable electronics, electric vehicles, home energy storage systems, and grid-level energy leveling solutions.^[1] The key characteristics of rechargeable LIBs are high energy and power densities that result from their reversible and efficient electrochemistry. However, growing demand for extending the range of electric vehicles and the battery life of portable devices has driven efforts to develop next-generation LIBs with higher capacities. Since the capacity of a LIB is primarily determined by its electrochemically active electrode materials, a considerable number of studies have attempted to identify alternative materials with higher reversible lithiation capacity.^[2] In particular, high-capacity cathode materials have been intensively

investigated since cathode materials generally exhibit significantly lower capacities than anode materials, leaving more room for improvement. The capacity of active electrode materials is quantified with two figures of merit: capacity per unit mass (i.e., specific or gravimetric capacity with typical units of mAh g^{-1}) and capacity per unit volume (i.e., volumetric capacity with typical units of mAh cc^{-1}). High specific capacities have traditionally been the target of electronic devices to enable improved portability, whereas high volumetric capacity is equally important in large-scale applications, such as electric vehicles and home energy storage systems, due to the limited space where large LIB packs can be mounted.^[1b,3]


Ni-rich layered cathodes, such as $\text{LiNi}_{0.8}\text{Co}_{0.15}\text{Al}_{0.05}\text{O}_2$ (NCA) and $\text{LiNi}_{0.8}\text{Co}_{0.1}\text{Mn}_{0.1}\text{O}_2$ (NCM), are among the most successful classes of LIB cathode materials due to their reversible gravimetric capacities approaching $\approx 200 \text{ mAh g}^{-1}$. This class of cathode materials surpasses the capacity limits of conventional LiCoO_2 (140 mAh g^{-1}) due to the increased range of Ni-based redox chemistry.^[4] Typically, these materials are synthesized as primary nanoparticles that then aggregate into a microscale secondary particle. As this scheme enables access to the large active surface area of the primary nanoparticles and the high

Dr. K.-Y. Park, Dr. J.-M. Lim, N. S. Luu, J. R. Downing, S. G. Wallace, L. E. Chaney, Dr. H. Yoo,^[†] Dr. W. J. Hyun, Dr. H.-U Kim, Prof. M. C. Hersam
Department of Materials Science and Engineering
Northwestern University
Evanston, IL 60208, USA
E-mail: m-hersam@northwestern.edu

Dr. H.-U Kim
SKKU Advanced Institute of Nanotechnology
Sungkyunkwan University (SKKU)
Suwon, Gyeonggi-do 16419, Korea

Prof. M. C. Hersam
Department of Chemistry
Northwestern University
Evanston, IL 60208, USA

Prof. M. C. Hersam
Department of Electrical and Computer Engineering
Northwestern University
Evanston, IL 60208, USA

 The ORCID identification number(s) for the author(s) of this article can be found under <https://doi.org/10.1002/aenm.202001216>.

^[†]Present address: Department of Electronics Engineering, Gachon University, 1342 Seongnam-daero, Seongnam 13120, Korea

DOI: 10.1002/aenm.202001216

packing density of the secondary microparticles, the volumetric capacity of Ni-rich cathode materials has been projected to reach ≈ 690 mAh per cc.^[4b] Additional higher-capacity cathode materials are also under development, such as rock-salt^[2a,5] and pure LiNiO₂ phases,^[2c] but their cyclic stability has not yet reached sufficient levels for most practical applications.

While the Ni-rich layered cathodes possess intrinsically high capacities, the actual volumetric and specific capacities of the entire electrode also depend on the inactive components. In addition to the active material, conventional LIB electrodes consist of a conductive additive (most commonly carbon black) and a polymer binder (typically polyvinylidene fluoride (PVF), polyvinylidene difluoride (PVDF), or carboxymethyl cellulose (CMC)). Furthermore, intraelectrode pores that provide lithium-ion pathways can occupy more than 25% of the total electrode volume.^[6] The conductive additive and electrode porosity play a central role in determining battery kinetics because they are responsible for electron and lithium-ion transport, respectively. The polymer binder is also critical for stable electrochemical cycling by promoting and maintaining adhesion of the carbon conductive additive to the active materials.^[7] Despite their importance, the goal is to minimize these inactive components since they compromise the overall electrode specific capacity. Even more concerning, the inclusion of inactive components significantly cuts down the volumetric capacity of the electrode due to the low tap density of traditional carbon additives as schematically depicted in **Figure 1a**. For example, the overall compressed density for a standard NCA electrode is significantly decreased from ≈ 3.6 to ≈ 2.9 g cc⁻¹ for a carbon black loading of 5 wt% (Table S1, Supporting Information), which is on the low end of typical conductive additive loadings in previous literature reports.^[8]

An enticing solution for maximizing both specific and volumetric capacity of LIB electrodes is to minimize the conductive additive loading. This strategy also has the potential to limit the loading of binders since the total surface area of the electrode components is reduced. However, it has proven difficult to construct LIBs that deliver acceptable electrochemical performance at low conductive additive loadings. To illustrate the challenge, **Figure 1b** shows a magnified schematic of an electrode with minimal loading of carbon black. Because the carbon black particles have a spherical shape with a typical diameter of ≈ 100 nm, a percolating electrical network is difficult to form unless a significant amount of carbon black is blended into the electrode to fill the interstitial space. Moreover, point contacts between the carbon black and active material particles lead to current concentration that cause resistive drops and over potential issues.^[8b,9] These issues tend to be exacerbated at industrially relevant active material areal loadings (≈ 10 mg cm⁻²) that require large electrode thicknesses.^[6a,10]

These limitations of particle-based conductive additives can potentially be overcome by an electrode design where each active material particle is coated with a thin electrically conductive coating (**Figure 1c**). In addition to achieving ultrahigh active material packing densities, this design reduces lithium-ion tortuosity since it minimizes the internal structural complexity of electrodes that incorporate carbon black particles.^[6b,11] Due to its high electrical conductivity, atomically thin nature, and compatibility with the electrochemical environment inside of LIBs, graphene is a leading candidate for coating active material particles. Assuming that graphene forms a conformal contact on the active material particle surface (**Figure 1d**), electron transport will be uniformly distributed, thus minimizing current crowding and electrode polarization. Although mass production

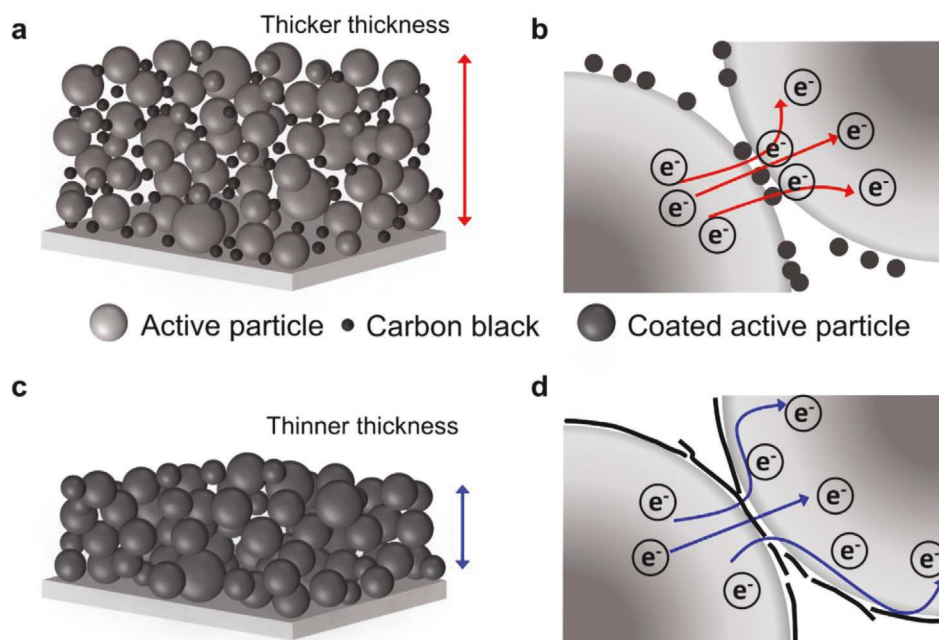


Figure 1. Comparison of point-contact and conformal planar-contact charge transport networks in lithium-ion battery electrodes. a) Schematic of a conventional electrode consisting of active materials and carbon black conductive agent. b) An inherently limited, point-contact electron transport pathway arising from particle-based carbon additives. c) Electrodes consisting of thin graphene-coated active particles with a high packing density. d) Conformal planar contacts minimize current bottlenecks and facilitate percolating pathways throughout the electrode.

of high-quality graphene has already been developed,^[12] the lack of scalable coating methods that result in conformally coated LIB active material particles has prevented the full realization of this strategy. For example, a recent study has shown that graphene balls can be blended with electrode materials via a milling process, but this method is not suitable for obtaining conformal coatings using graphene flakes.^[13] Similarly, other previously attempted schemes for blending graphene with LIB active material particles have either resulted in insufficient electrical conductivity (and thus the need to still add carbon black conductive additives)^[14] or crumpling of graphene,^[15] both of which lead to poor tap densities and compromised volumetric capacities.

Here, we overcome these limitations and achieve conformal, ultrathin, conductive graphene coatings on LIB active materials particles using a scalable Pickering emulsion method. Since this approach employs high-quality, solution-exfoliated graphene that possesses exceptional electrical conductivity, only 0.5 wt% graphene is required to achieve high electrochemical performance in thick electrodes that possess industrially relevant active material areal loadings ($\approx 11 \text{ mg cm}^{-2}$). Due to the exceptionally low inactive material loading, the resulting NCA electrodes achieve specific and volumetric capacities within $\approx 98\%$ of the theoretical limits for NCA materials. The efficient electron and lithium-ion transport in these electrodes also leads to superlative rate capability, while the conformal graphene coating mitigates electrochemical degradation mechanisms and consequently enhances cycle life. While demonstrated here for NCA cathodes, this Pickering emulsion coating scheme can likely be generalized to other active material particles, thus providing a pathway to theoretical specific and volumetric capacities in practical LIB electrodes.

2. Results and Discussion

2.1. Conformal Graphene Coatings via Pickering Emulsion Processing

Pickering emulsions result from two immiscible solvents, where solid-state emulsifiers stabilize the interfaces of the emulsion droplets. Because of its benefits for mass production and controllability, Pickering emulsions have been previously utilized in batteries for in situ polymerization^[16] and hollow carbon structures.^[17] In our experiments, as the first step in achieving a conformal graphene coating, a Pickering emulsion was formed using acetonitrile and hexane as immiscible solvents and graphene (Gr) as a solid-state emulsifier as schematically shown in **Figure 2a**. The conditions of the Pickering emulsion were chosen such that the lower boiling point solvent (i.e., hexane: boiling point = 68°C) resides in the interior of the emulsion droplets with the higher boiling point solvent (i.e., acetonitrile: boiling point = 82°C) as the exterior solvent. In addition, ethyl cellulose (EC) was used as an additive for increasing the dispersity and emulsifier characteristics of graphene. Since NCA particles disperse preferentially in hexane compared to acetonitrile, the NCA particles resided in the interior of the emulsion droplets. The choice of solvents for the Pickering emulsion was based on compatibility with NCA

(Figures S1 and S2, Supporting Information) in addition to the low and different boiling points that facilitate the formation of a homogenous graphene coating as will be discussed further below.

The detailed procedure for forming the Pickering emulsion begins by dispersing graphene into acetonitrile to form a base solution. With regard to the dispersibility of graphene in acetonitrile, it is worth noting that there is still debate over whether the surface chemistry of graphene is hydrophobic or hydrophilic,^[18] but it is generally observed that graphene itself is difficult to disperse in many solvents including ethanol, water, and acetonitrile. However, previous studies have demonstrated that stable graphene dispersions can be prepared in ethanol by using EC as a stabilizer.^[19] Similarly, we found that graphene can be effectively dispersed in acetonitrile using EC. **Figure 2b** shows the degree of dispersion of graphene in acetonitrile as a function of the relative weight ratio of graphene to EC. The graphene itself was derived from liquid phase exfoliation using a previously published procedure.^[19] As shown by atomic force microscopy (AFM) in **Figure 2c**, the multilayer graphene flakes possess an average lateral size of $\approx 160 \text{ nm}$ and an average thickness of $\approx 3 \text{ nm}$ (AFM histogram provided in **Figure S3** in the Supporting Information). When graphene was dispersed alone in acetonitrile at a concentration of 0.275 mg mL^{-1} or with a 1:1 weight ratio of EC (in this case, the concentration of EC is also 0.275 mg mL^{-1}), graphene aggregation occurred within 24 h following horn ultrasonication as shown in the lower panels of **Figure 2b**. On the other hand, when the relative amount of EC was increased (i.e., graphene:EC ratio of 1:2), the resulting graphene dispersion was stable without aggregation for over 1 week.

The optimal 1:2 Gr/EC dispersion in acetonitrile formed a Pickering emulsion once immiscible hexane solvent was added. Specifically, **Figure 2d** shows a series of 5 mL Gr/EC in acetonitrile dispersions with decreasing volumes of hexane (left to right, 4–1 mL of hexane) following one minute of vortex mixing. The concentrations of Gr and EC in acetonitrile were 0.275 and 0.55 mg mL^{-1} , respectively. All acetonitrile/hexane (A/H) mixtures showed graphene separation into a top layer in addition to the formation of floating emulsion droplets, which were stable in size for one week. Since the density of hexane (0.65 g mL^{-1}) is lower than acetonitrile (0.79 g mL^{-1}), it can be deduced that the interior solvent of the floating droplets is hexane rather than acetonitrile. Consistent with this interpretation, the average size of the emulsion droplets was reduced with decreasing hexane content (**Figure 2e**). Emulsion droplets with diameters exceeding $100 \mu\text{m}$ were observed at a 5:4 ratio of acetonitrile to hexane, whereas the emulsion droplet diameter dropped to less than $5 \mu\text{m}$ at a 5:1 ratio of acetonitrile to hexane (**Figure S4**, Supporting Information). Further reduction in the emulsion droplet size was not observed for even lower hexane content (**Figure S5**, Supporting Information). Moreover, the concentration of graphene also altered the average size of the emulsion droplets (**Figure S6**, Supporting Information), which is an observation that is consistent with other Pickering emulsions.^[20]

After preparing the Pickering emulsion, NCA particles were inserted into the emulsion droplets. Given the actual surface area of graphene obtained by the solution–exfoliation process^[19]

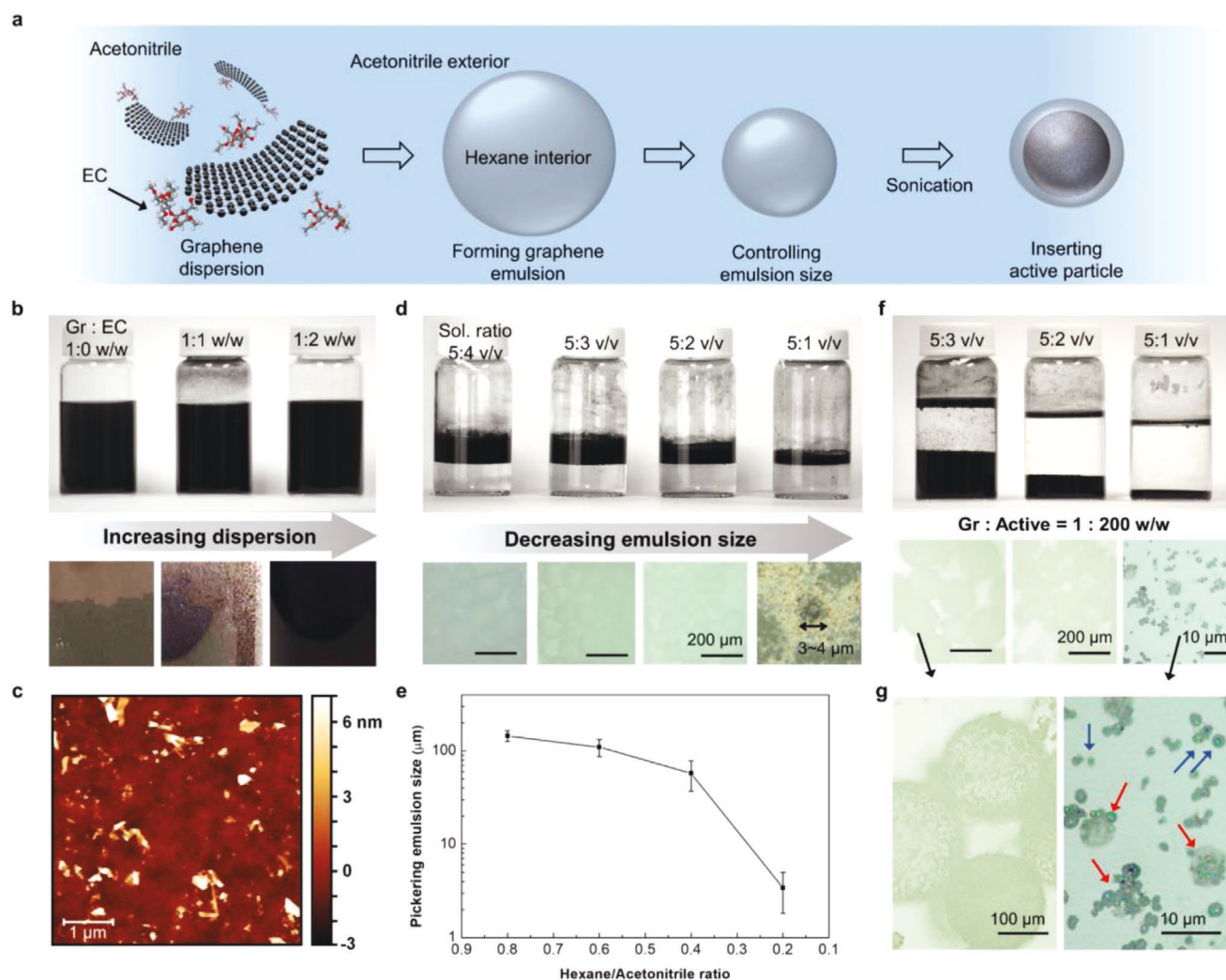


Figure 2. Graphene Pickering emulsions based on acetonitrile and hexane. a) Schematic of the Gr/EC Pickering emulsion in acetonitrile and hexane followed by insertion of the active material particle. b) Dispersion behavior of graphene in acetonitrile depending on Gr:EC (w/w) ratio. Inset figures show magnified images of the dispersion quality. c) Atomic force microscopy image of pristine graphene flakes obtained by liquid phase exfoliation. d) Hexane droplets formed in Gr/EC/acetonitrile solution, where the volume ratio of acetonitrile to hexane is (from left to right) 5:4, 5:3, 5:2, and 5:1. The graphene concentration in acetonitrile is fixed as 0.275 mg cc^{-1} . e) Size change of emulsion droplets with changing hexane to acetonitrile volume ratio. f) Encapsulation of NCA active particles by emulsion droplets, where the volume ratio of acetonitrile to hexane is (from left to right) 5:3, 5:2, and 5:1 with a graphene concentration in acetonitrile of 0.275 mg cc^{-1} . The weight ratio of graphene to NCA is 1:200. g) Magnified optical microscopy images of encapsulated NCA particles acetonitrile to hexane ratios of (left) 5:3 and (right) 5:1.

(Figure S3, Supporting Information) and the average NCA particle size (Figure S7, Supporting Information), the ideal weight ratio of graphene to NCA was determined to be 1:200. Accordingly, 550 mg of NCA powder was added to 10 mL of the graphene/acetonitrile solution (0.275 mg mL^{-1}), and A/H solutions were prepared with ratios of 5:3, 5:2, and 5:1 (left to right in Figure 2f) via bath sonication. Video S1 in the Supporting Information shows the NCA particle insertion process using bath sonication with a 5:1 A/H solution. Initially, the emulsion mixture with NCA was homogeneously distributed following bath sonication for 10 min. However, when the emulsion mixture was then shaken or subjected to vortexing, graphene emulsion droplets immediately formed and sedimented with NCA powders across all A/H ratios as shown in Figure 2f. In contrast, the mixture without hexane or NCA powder did not

show this behavior (Videos S2 and S3 in the Supporting Information, respectively). The sedimentation of the emulsion droplets suggests the insertion of the relatively dense NCA particles, which is confirmed by optical microscopy (inset of Figure 2f,g). Once the NCA particles were inserted, the emulsions remained stable for more than a week.

The right panel of Figure 2g shows the insertion of NCA particles into an emulsion with an A/H ratio of 5:1, where the size of most droplets is less than $5 \mu\text{m}$. In this case, the emulsion droplets encapsulate individual NCA particles (blue arrows) or a relatively small number of NCA particles (red arrows). When tracking the droplet/particle complex during drying, clear reductions in droplet size are observed as shown in Figure S8 (Supporting Information), ultimately resulting in the particles being conformally coated with

graphene as confirmed by scanning electron microscopy (SEM; Figure S9, Supporting Information). This conformal encapsulation is enabled by two factors. First, the stable average size of droplets at a 5:1 A/H ratio is less than 5 μm , which corresponds to the size of individual NCA particles. Second, the NCA particles and the emulsion graphene shells favorably interact, resulting in efficient formation of Pickering emulsion droplets around each NCA particle. In particular, as shown in Video S1 (Supporting Information), Pickering emulsion droplets form promptly upon agitation when NCA particles are present, whereas the mixture without NCA particles formed emulsion droplets much more slowly (Video S3, Supporting Information).

The drying process needs to be carefully controlled in order to achieve a conformal graphene coating on the NCA particles. For example, when the optimized Pickering emulsion with NCA particles was dried without precise control at standard temperature and pressure (STP), the droplets prematurely burst, resulting in an uneven graphene coating on the NCA particle surface as schematically shown on the left side of Figure 3a. The optical microscopy image in Figure 3b shows the results of

this uncontrolled STP drying process, where residual graphene flakes are spread around the NCA particles following premature bursting of the emulsion droplets. On the other hand, a conformal graphene coating on the NCA particles is achieved by selective evaporation of the interior hexane solution through fractional distillation as schematically shown on the right side of Figure 3a. This controlled fractional distillation is achieved with a rotary evaporator, where the bath temperature was set to 50 $^{\circ}\text{C}$ (Figure S10, Supporting Information). After 20 min at 0.6 atm pressure (Figure 3d), the hexane is completely and selectively removed, resulting in a controlled collapse of the emulsion droplets and a conformal graphene coating on the NCA particles. Following removal of the hexane, the resulting dispersion that consists of graphene-encapsulated NCA powders in acetonitrile shows exceptional stability. In particular, even upon stirring, the NCA powder is not separated from the graphene coating (Figure S11, Supporting Information). Further lowering the pressure in the rotary evaporator to under 0.2 atm results in full removal of the acetonitrile (Figure 3d), leading to fully graphene-coated NCA particles. As shown in Figure 3e–h, SEM characterization confirms the effectiveness of fractional

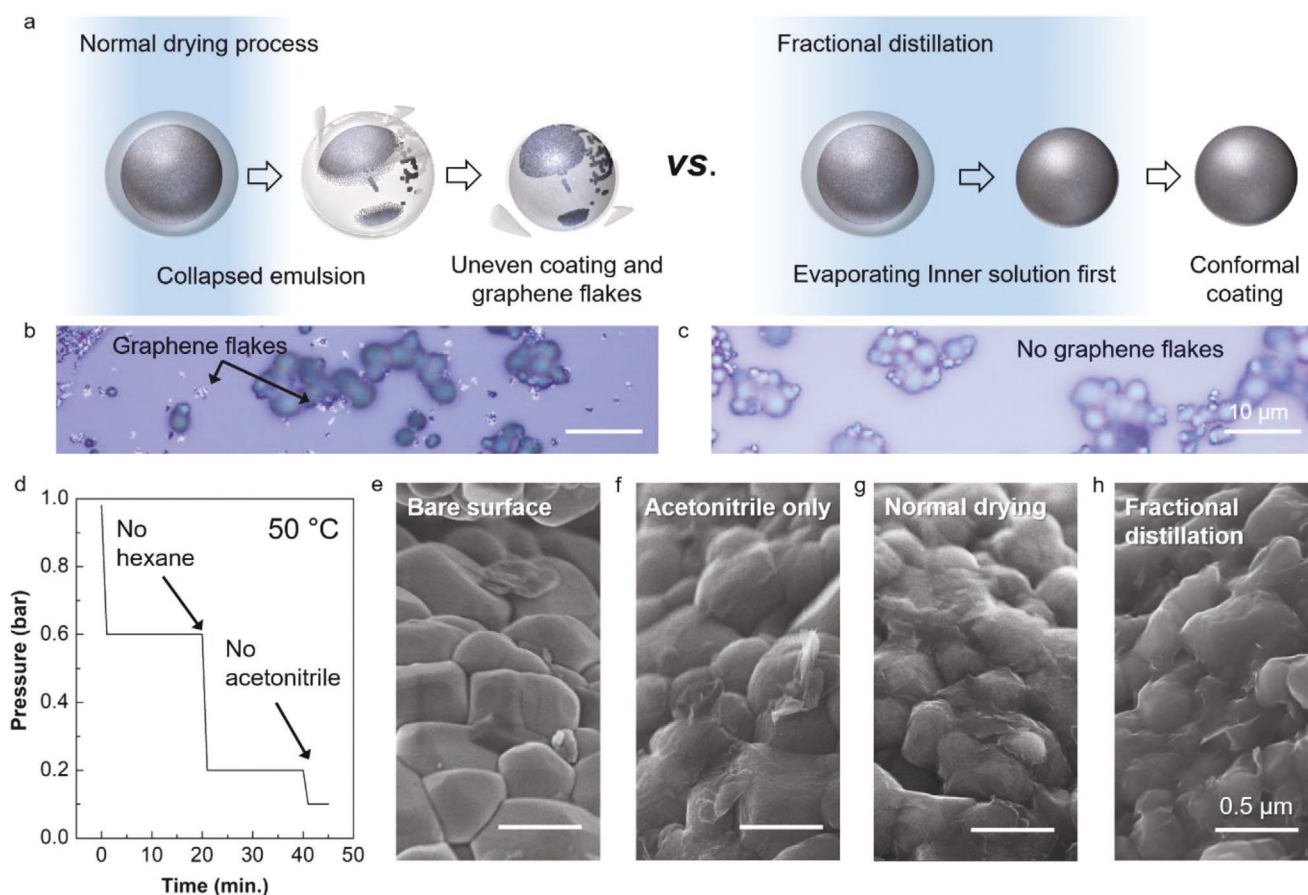


Figure 3. High graphene coating uniformity by fractional distillation. a) Schematic comparison of the coating uniformity depending on the drying process: left) normal drying process and right) fractional distillation drying process by evaporating hexane and acetonitrile sequentially. Optical microscopy images of dried powders by b) normal process and c) using fractional distillation. d) Chamber pressure as a function of time during fractional distillation. The heated bath is set at 50 $^{\circ}\text{C}$. Scanning electron microscopy images showing NCA particles prepared by the following methods: e) bare active material surface; f) single solvent process using Gr/EC dispersed in acetonitrile with normal drying on a hot plate at 50 $^{\circ}\text{C}$; g) Pickering emulsion process with normal drying on a hot plate at 50 $^{\circ}\text{C}$; h) Pickering emulsion process with drying by fractional distillation.

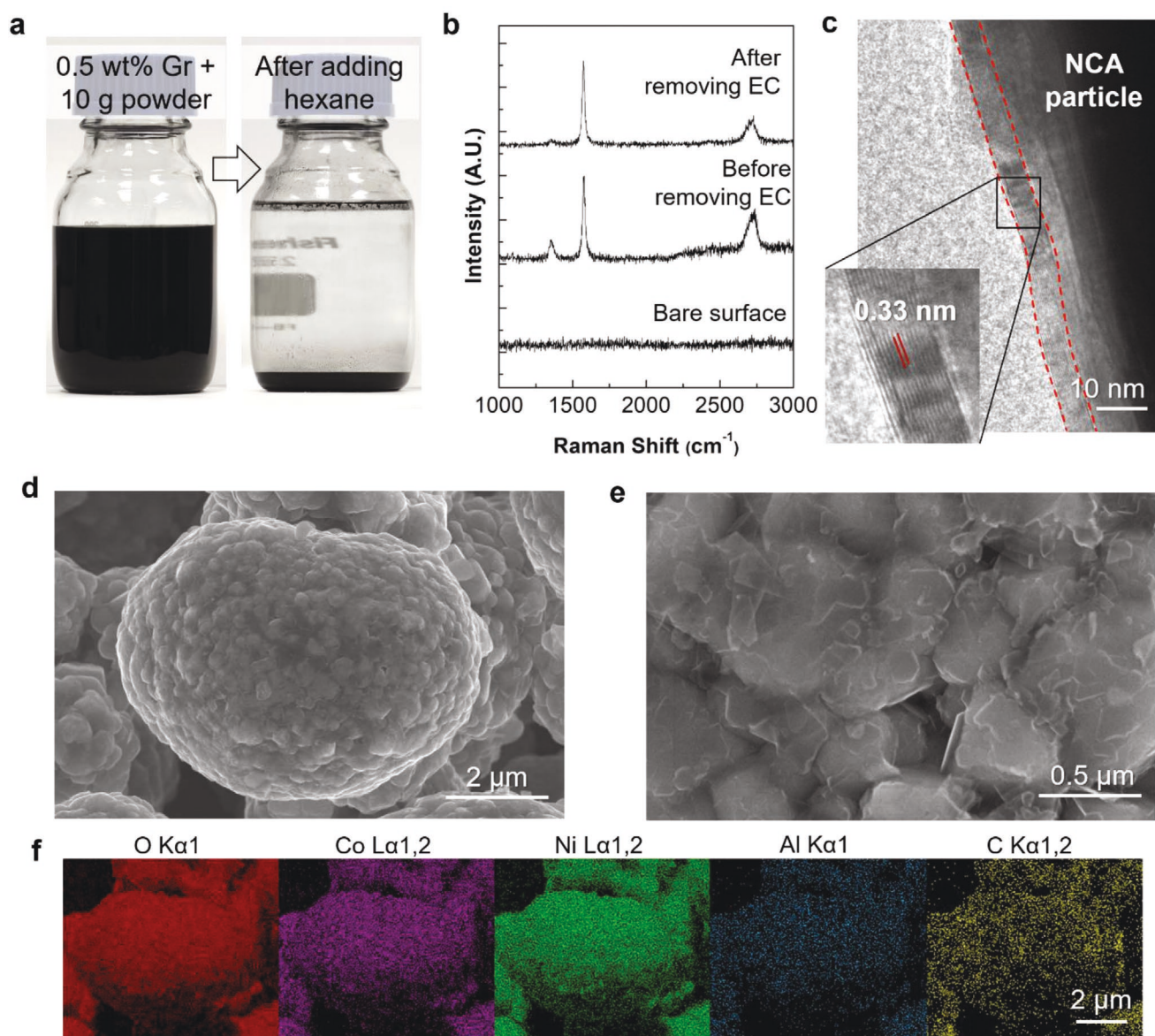


Figure 4. Scaled-up coating and characterization following ethyl cellulose (EC) removal. a) Scaled-up Pickering emulsion process for conformally coating 10 g of NCA powder with graphene. b) Raman spectra of the coated powder before removing EC, after removing EC through thermal annealing at 250 °C in an oxidizing environment, and bare NCA. c) Transmission electron microscopy image of a graphene-encapsulated NCA particle, revealing conformal graphene flakes on the surface. d) Scanning electron microscopy (SEM) image of a graphene-encapsulated particle and e) a magnified SEM image showing the coating morphology. f) Energy-dispersive spectroscopy results for O, Co, Ni, Al, and C elements on a graphene-coated NCA particle following EC removal.

distillation in achieving a conformal graphene coating on the NCA particles.

Another advantage of the Pickering emulsion graphene coating scheme is its scalability. **Figure 4a** shows 10 gram-scale processing of NCA powder, which begins by dispersing the NCA powder in ≈ 180 mL of graphene dispersed in acetonitrile, where the weight ratio of graphene to NCA is 1:200. Before adding hexane (**Figure 4a**, left), the graphene is well dispersed in acetonitrile, but the NCA particles sediment and separate from the mixture. Following the addition of 36 mL of hexane and bath sonication for 10 min, Pickering emulsion droplets form and sediment (**Figure 4a**, right) in a manner

analogous to **Figure 2f**. Subsequent fractional distillation results in NCA powders that are conformally coated with graphene. Since the hexane and acetonitrile solvents are extracted separately through fractional distillation, these solvents can be easily recycled for subsequent Pickering emulsions. In total, the entire coating process takes less than 2 h until the graphene-coated NCA powder is completely dried. Due to its scalability, high throughput, and amenability to recycling, the Pickering emulsion process can be straightforwardly applied to large-scale manufacturing.

Following fractional distillation, the conformal coating on the NCA powder consists of graphene and EC. While the

presence of EC may be acceptable or perhaps even desirable in some applications, it impedes lithium-ion and electron transport and thus needs to be removed for LIBs. It is well known that EC is thermally decomposed in oxidizing environments at mild temperatures of $\approx 250^\circ\text{C}$,^[21] which is an annealing condition that is compatible with graphene and active materials in LIBs.^[22] Indeed, differential thermal analysis (DTA) and thermogravimetric analysis (TGA) show that the residual EC can be removed following thermal annealing at 250°C in an O_2 atmosphere (Figure S12, Supporting Information). Further evidence for EC removal is provided by Raman spectroscopy (Figure 4b), where a noticeable reduction in the D band is observed after annealing, which is consistent with previous studies of EC pyrolysis in the presence of graphene.^[23] Overall, thermal annealing removes the vast majority of EC, with the remaining amorphous carbon residue possessing a high sp^2 -carbon content that facilitates electron transport between the graphene flakes.^[23] Transmission electron microscopy (TEM) and SEM in Figure 4c–e and Figure S13 (Supporting Information) confirm that the final coating is highly conformal and consists of ≈ 10 nm of well-defined graphitic carbon. Moreover, energy-dispersive spectroscopy (EDS) elemental mapping verifies the homogeneity of the carbon coating as shown in Figure 4f and Figure S15 (Supporting Information), whereas the pristine NCA particles show virtually no carbon signal (Figure S16, Supporting Information).

2.2. Electrochemical Characterization

LIB cathodes with an unprecedentedly low conductive additive loading were fabricated using the graphene-coated NCA powders. In particular, a mixture of graphene-coated NCA and PVDF binder were cast on an aluminum current collector in a weight ratio of 99.2:0.8, which implies that the overall composition of NCA, graphene, and PVDF was 98.7:0.5:0.8. A high active material areal loading of $\approx 11\text{ mg cm}^{-2}$ was used to demonstrate the suitability of the graphene-coated NCA powders for practical LIBs.^[6a,10b] Two control group electrodes were prepared with different ratios: one with the same carbon additive ratio (i.e., NCA, carbon black, and PVDF in a ratio of 98.7:0.5:0.8) and another with an order of magnitude higher amount of carbon black (i.e., NCA, carbon black, and PVDF in a ratio of 90:5:5). The prepared electrodes were compressed utilizing a commercial rolling apparatus until just before cracks appeared in the films. The 5 wt% carbon electrode had a serious adhesion issue for PVDF binder levels less than 3 wt%, but the 0.5 wt% graphene and 0.5 wt% carbon black electrodes showed excellent adhesion even with only 0.8 wt% binder (Figure S17, Supporting Information). This result shows that the reduction in carbon additive ratio reduces the essential amount of binders, while concurrently increasing the actual specific and volumetric capacity of the electrodes. SEM images in Figure 5a show that the thicknesses of the 0.5 wt% graphene, 0.5 wt% carbon black, and 5 wt% electrodes were ≈ 30 , ≈ 30 , and $\approx 37\text{ }\mu\text{m}$, respectively. The compressed electrode densities were $\approx 3.6\text{ mg cc}^{-1}$ for the 0.5 wt% graphene and 0.5 wt% carbon black electrodes, and 2.9 mg cc^{-1} for the 5 wt% carbon black electrode (Table S1, Supporting Information). The compressed electrode density

of 3.6 mg cc^{-1} exceeds the previously highest reported density using NCA materials ($\approx 3.3\text{ mg cc}^{-1}$) and can be attributed to the exceptionally low carbon content enabled by the conformal graphene coating.^[4b]

Short lithium-ion diffusion lengths and well-percolating electron transport pathways are ideal attributes for a LIB electrode. Since the 0.5 wt% graphene and 0.5 wt% carbon black electrodes were thinner and contained little to no porous carbon compared with the 5 wt% carbon black electrode, the lower carbon content electrodes are expected to have reduced tortuosity for lithium-ion diffusion.^[6b,11] In addition, the conformal graphene coating is beneficial for forming percolating electron transport pathways since the coating can provide a seamless electrical network, even across multiparticle contacts. Moreover, the high electrical conductivity of graphene coupled with its conformal coating geometry is expected to minimize the overall contact resistance to the NCA particles. Top-view SEM images of the electrodes confirm the expected differences in the amount of carbon particles present (Figure 5b; Figure S18, Supporting Information) with the 0.5 wt% electrodes consisting almost exclusively of active NCA particles.

To investigate the electronic properties of the as-prepared electrodes, electrical conductivity was measured using the four-point probe method with the results tabulated in Table 1. The electrodes with 0.5 wt% graphene possessed $\approx 80\%$ of the electrical conductivity of the 5 wt% carbon black electrode despite having an order of magnitude less carbon, unlike the 0.5 wt% carbon black electrode that was more than a factor of 2 less conductive. The conformal graphene coating also facilitates charge transport kinetics at the active electrode surface. Figure 5c shows the Nyquist plots of lithium metal two-electrode cells after one activation cycle. The Nyquist plots exhibit two semi-circles, which is typical for layered cathode electrodes and has been attributed to two different charge transfer processes at the surface.^[24] The graphene-coated NCA electrode showed a significant reduction in R_{ct1} and R_{ct2} compared to the other electrodes (inset of Figure 5c) as summarized in Table 1, thus confirming improved charge transfer kinetics.

The electrochemical properties of the as-prepared electrodes were further evaluated using lithium metal half-cells. Figure 5d presents the galvanostatic profiles of the electrodes at a C/10 rate in the first cycle. The gravimetric capacity of the electrodes was determined not only from the weight of the active materials, but also including the weight of the binder and carbon component in order to focus on the overall electrode capacity. A large irreversible capacity appeared in the first cycle for all electrodes as is typically observed for Ni-rich layered oxide cathodes.^[4b,25] The first discharge capacity of the 0.5 wt% graphene electrode was 191 mAh g^{-1} , whereas the 0.5 and 5 wt% carbon black electrodes showed 179 and 185 mAh g^{-1} , respectively. The gravimetric capacity of NCA itself is typically $\approx 195\text{ mAh g}^{-1}$ for the first discharge.^[4b,26] Impressively, the 0.5 wt% graphene electrode achieved 98% of this value even considering all of the inactive components, whereas the 0.5 and 5 wt% carbon black electrodes showed lower practical capacities due to limited electronic transport and a large portion of inactive components, respectively. In addition, an overshooting at the $\approx 3.7\text{ V}$ shoulder appeared in the initial charging profile of

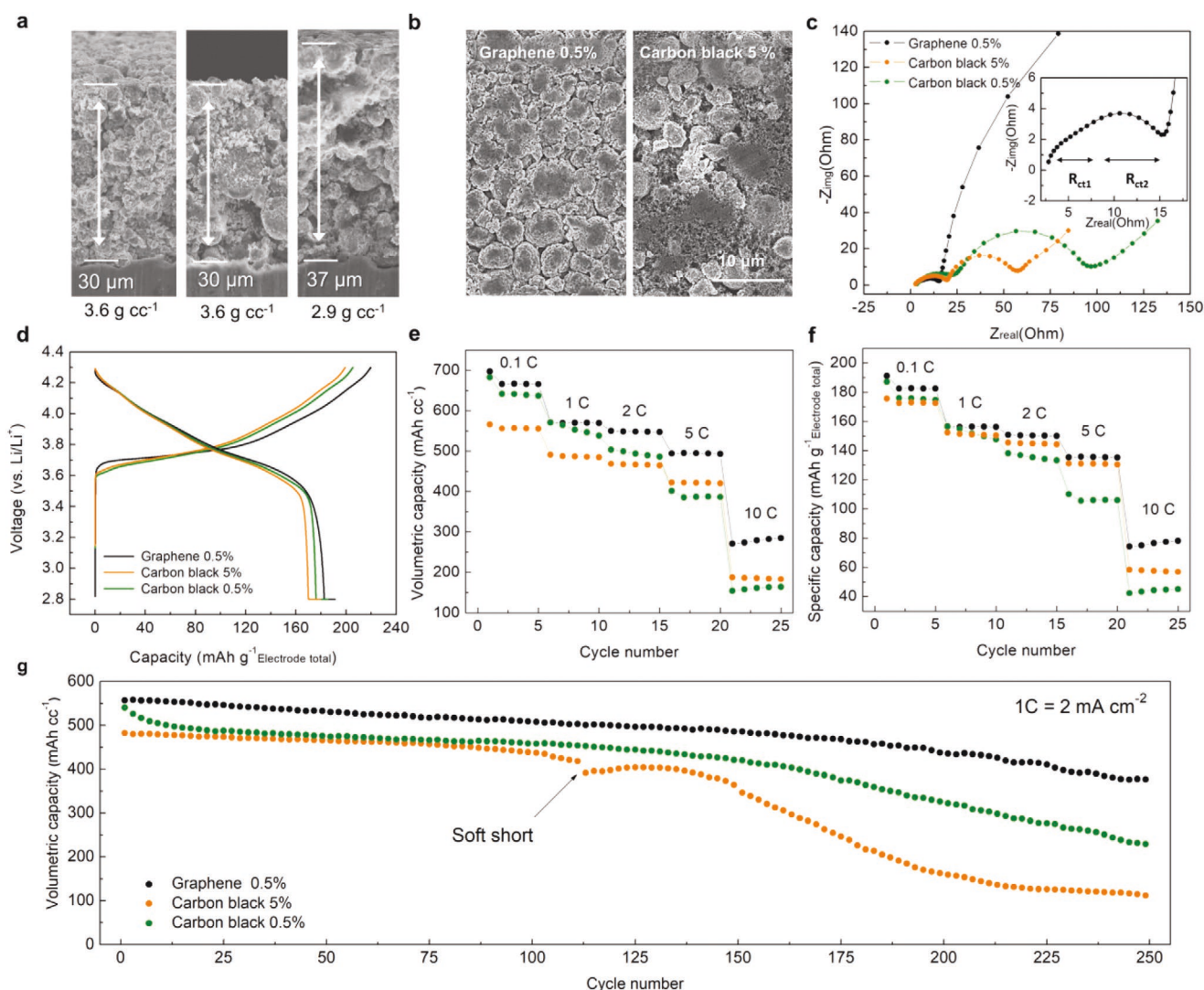


Figure 5. Electrochemical testing of NCA electrodes. a) Compressed thickness of electrodes consisting of (left) 0.5 wt% graphene, (middle) 0.5 wt% carbon black, and (right) 5 wt% carbon black electrodes. b) Top-view scanning electron microscopy images of 0.5 wt% graphene and 5 wt% carbon black electrodes. c) Nyquist plots of prepared electrodes. d) Galvanostatic profiles of prepared electrodes with a current density of $C/10$. A constant voltage was applied at 2.8 V after discharge until the current density reached $C/50$. e) Rate capability results with respect to volumetric capacity. The electrodes were charged to 4.3 V at a 1C rate and discharged to 2.8 V at rates of 1C, 2C, 5C, and 10C (except for the $C/10$ test). f) Rate capability results with respect to the total electrode specific capacity. g) Cycle life test results at a rate of 1C.

Table 1. Comparison of NCA electrode charge transport properties for different carbon loadings.

Electrode ^{a)}	Resistivity [Ω cm]	Conductivity [Ω cm ⁻¹]	R_{ct1} [Ω]	R_{ct2} [Ω]
Graphene 0.5%	0.72 ± 0.14	1.45 ± 0.34	3.9	10.2
Carbon black 0.5%	1.22 ± 0.25	0.85 ± 0.19	24.2	72.4
Carbon black 5%	0.54 ± 0.03	1.86 ± 0.11	17.7	38.6

^{a)} Resistivities and conductivities of the prepared electrodes were measured by the four-point probe method. The average conductivities were obtained from five measurements for each electrode. Deconvoluted impedances of the first (R_{ct1}) and second (R_{ct2}) charge transfer at the surface as obtained by electrochemical impedance spectroscopy.

the 0.5 wt% graphene electrode as is commonly observed for other coated LIB materials.^[25,27]

The rate capability of the 0.5 wt% graphene electrode outperformed the other electrodes for both volumetric capacity and total electrode gravimetric capacity (Figures 5e,f). The volumetric capacity of the 0.5 wt% graphene electrode was at least 20% higher than the 5 wt% carbon black electrode for all tested current densities as shown in Figure 5e. This improved volumetric capacity results from the replacement of bulky carbon black with the conformal graphene coating that significantly increases the compressed electrode density. Although the 0.5 wt% carbon black electrode also delivered a high compressed electrode density, it showed much lower rate

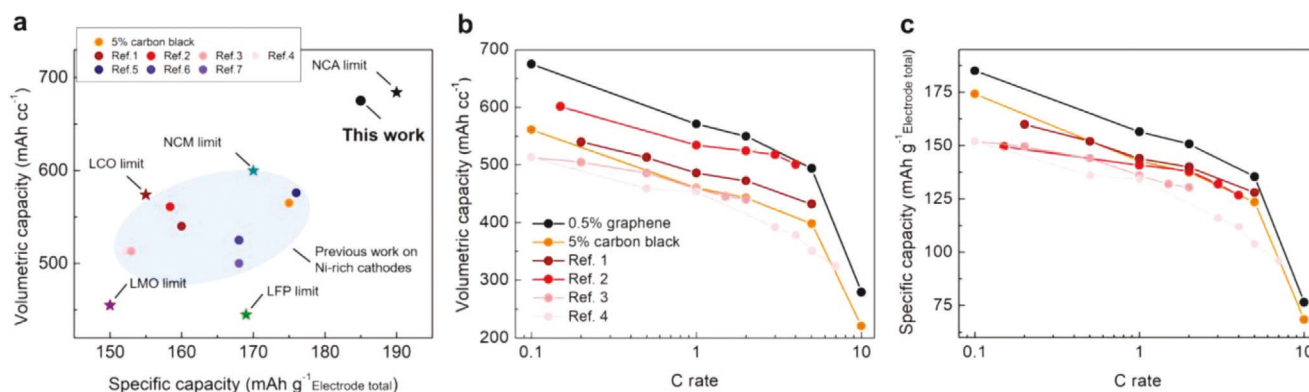


Figure 6. Comparison of volumetric and specific capacities with theoretical limits and literature precedent. a) The volumetric and specific capacity of this work is compared to theoretical limits (star-shaped points) and literature precedent (round points) for various cathode materials. Comparison of rate performance results with literature precedent for b) volumetric and c) specific capacity. The references are defined as follows: ref. [1] used Mn content control,^[29c] ref. [2] used Al gradient doping,^[29a] ref. [3] used particle growth control,^[31] ref. [4] used preoxidized precursor,^[29b] ref. [5] used vanadium treatment,^[32] ref. [6] used NaAlO₂ treatment,^[32] and ref. [7] used morphology control.^[33] For the papers that do not provide compressed/packing densities, the density was estimated based on the amount of conductive carbon additive and binder used.

capability due to its poor electronic percolation. The 0.5 wt% graphene electrode shows similar rate capability advantages for the case of total electrode gravimetric capacity. The galvanostatic profiles of all electrodes are presented in Figure S19 (Supporting Information). Previous studies have revealed that electrochemical reactions of relatively high-loading electrodes are limited by lithium-ion diffusion in the electrolyte at high C-rates.^[10b,28] Consequently, even higher rate performance up to 20C can be achieved for the 0.5 wt% graphene electrode by reducing the areal loading to $\approx 6 \text{ mg cm}^{-2}$ (Figure S20, Supporting Information).

The 0.5 wt% graphene electrode also possessed outstanding cycle retention as shown in Figure 5g. In the case of the 0.5 wt% carbon black electrode, the capacity retention at 1C was significantly compromised within the first 10 cycles, which can likely be attributed to an insulating SEI layer on the surface that leads to irreversible degradation of the electronic network. On the other hand, the 5 wt% carbon black and 0.5 wt% graphene electrodes retained 90.5% and 91.5% of their initial volumetric capacities, respectively, over 100 cycles (Figure 5g) while also maintaining $\approx 99.7\%$ Coulombic efficiency (Figure S21, Supporting Information). However, a sudden soft short circuit profile was consistently observed in the 5 wt% carbon black preceding 125 cycles, whereas the 0.5 wt% graphene electrode could be still cycled over 250 times while retaining $\approx 70\%$ of its initial capacity. Previous studies have shown that high-loading electrodes ($>10 \text{ mg cm}^{-2}$) usually maintain lower than 80% of the initial capacity after 100 cycles.^[29] Furthermore, studies based on high-loading electrodes rarely report more than 100 cycles due to the potential for serious current concentration even with a small amount of accumulating side reaction in the electrode.^[10b] The world-class cycling performance of the 0.5 wt% graphene electrode originates from its simplified electrode structure and the chemical inertness of graphene that minimizes side reactions, such as electrolyte decomposition and transition metal dissolution.^[30]

Figure 6 compares the electrochemical results of this study to theoretical limits and the best previously reported LIB cathodes in the literature. In particular, the star-shaped markers in

Figure 6a represent the practically achievable volumetric and specific capacity limits of LIB electrodes based on the most common cathode materials: LiFePO₄ (LFP), LiCoO₂ (LCO), NCM, and NCA. These limits correspond to the theoretical specific capacities of the active materials, which can only be achieved at the electrode level without any binders or conductive additives, whereas the volumetric capacities assume the ideal crystal density with 25% porosity for lithium-ion diffusion, which is the experimentally observed porosity limit in extremely compressed electrodes.^[6b] Among the plotted data points, nickel-rich cathodes show the most promise for high specific and volumetric capacities due to the advantages of Ni-redox chemistry.^[4b] However, current electrode engineering strategies have been unable to achieve performance close to the theoretical limit of these high capacity cathode materials as shown for the round markers that depict the results of previous studies on NCA and NCM. On the other hand, the 0.5 wt% graphene electrode reaches $\approx 98\%$ of its volumetric and specific capacity limits.

Not only does the 0.5 wt% graphene electrode push the limits of volumetric and specific capacity, but it also achieves unprecedented rate performance. Figures 6b,c show comparisons of the volumetric and specific rate capability, respectively, compared to previous best-in-class results for Ni-rich cathodes. For a reliable comparison, the results in Figures 6b,c only include studies with an areal loading density of at least 7 mg cm^{-2} . The volumetric capacity of the 0.5 wt% graphene electrode (Figure 6b) showed an increase of at least 10% at all current density ranges, with an exceptionally high volumetric capacity of 500 mAh cc^{-1} being attained at a 5C rate. Moreover, as shown in Figure 6c, the total electrode specific capacity also delivered superior performance at all current densities. This superlative rate performance again confirms the exceptional electron and lithium-ion transport characteristics provided by electrodes based on conformal graphene coatings.

3. Conclusions

In this study, we have introduced a highly conformal graphene coating method based on Pickering emulsion processing. This

methodology can likely be employed in a manufacturing setting due to its high scalability, throughput, and amenability to recycling. The resulting conformal graphene coating allows the amount of carbon conductive additive in LIB electrodes to be substantially reduced without compromising electronic transport pathways. Correspondingly, the polymer binder level can also be reduced, leading to an exceptionally high active material percentage and packing density. The resulting electrodes show unprecedentedly high practical volumetric and specific capacities that approach theoretical capacity limits at high areal loadings. Furthermore, the efficient electron and lithium-ion transport in these electrodes implies superlative rate capability, while the conformal graphene coating mitigates degradation pathways that result in exceptional cycle life. While shown here to be particularly effective for LIB electrodes, the Pickering emulsion processing scheme can likely be generalized for the coating of a diverse range of particles with graphene and related 2D materials.

4. Experimental Section

Preparation of Graphene: Exfoliation of graphite was implemented by mixing 6000 g of flake graphite and 200 g of 4 cP EC, both from Sigma Aldrich, in a reservoir tank containing 5 L of 200-proof ethanol (Decon Labs, Fisher Scientific Co.). This mixture was continuously cycled through a 200 L inline shear mixer (Silverson Machines). After 23 h, the obtained mixtures were centrifuged with an Avanti J-26 XPI centrifuge using a JLA 8.1000 rotor, both from Beckman Coulter Inc., at 6500 rpm for 0.5 h. The ethanol-based supernatant containing polydisperse graphene with EC was then collected and flocculated by adding NaCl saltwater. The sedimented solids of graphene, EC, and salt were collected, combined in a 1 L Büchner funnel, and repeatedly washed with deionized water. The solid material was then transferred to a Pyrex container and dried under ambient conditions using a 150 W infrared lamp to fully dehydrate the sample. The dried graphene and EC mixture were dispersed in acetonitrile (Sigma Aldrich) using horn sonication at 30–40% amplitude for 1 h.

Sample Characterization: X-ray diffraction (XRD) patterns were measured using Scintag with Cu K α radiation ($\lambda = 1.5406 \text{ \AA}$). The acceleration voltage was 40 kV with a 20 mA current. The patterns were collected with a 2θ scan mode from 10° to 70° . The coating was imaged and confirmed by SEM (Hitachi SU8030) and TEM (JEOL ARM 200CF).

Electrode Fabrication and Electrochemical Testing: The NCA powder was procured from BASF TODA (HED NCA-1050, lot 1270203). Slurries for the electrode were blended with active materials (NCA or graphene-coated NCA), carbon black (MTI corporation, EQ-Lib-SuperP), and PVDF binder (corporation, EQ-Lib-PVDF) with *N*-methyl-2-pyrrolidone (NMP) using a planetary centrifugal mixer for 15 min. The mixed slurry was cast on aluminum foil with an areal loading of $\approx 11 \text{ mg cm}^{-2}$. The electrodes were dried in a 120°C oven for 20 min and compressed by a roller press (MTI, MSK-HRP-MR100DC). In order to maximize the compressed density, the electrodes were carefully compressed at least three times with a minimum rolling speed of 5 mm s^{-1} . The gap between the rollers was set as 40 and $50 \text{ }\mu\text{m}$ for the 0.5 wt% graphene/carbon black and 5 wt% carbon black electrodes, respectively. CR2032 coin cells were assembled with lithium metal (MTI Corporation, reference electrode), glass fiber (Whatman, separator), and 1.0 M LiPF $_6$ in ethylene carbonate/dimethyl carbonate of 1:1 volume ratio for rate capability testing (Sigma Aldrich, EC/DMC, electrolyte) or 1.2 M LiPF $_6$ in ethylene carbonate/ethyl methyl carbonate of 3:7 volume ratio with 2 wt% of vinylene carbonate for cycle retention testing (Sigma Aldrich, EC/EMC, electrolyte). Electrochemical testing was conducted with an Arbin battery cycler within the voltage range of 2.8–4.3 V versus Li/Li $^+$. Here, 1C of NCA is defined as 180 mA g^{-1} . An activation cycle was implemented

over a voltage range of 2.8–4.3 V with a current density of C/10. After the activation cycle, a constant potential of 2.8 V was applied until the current density reached C/50. Electrochemical impedance spectroscopy was performed using a Biologic VSP Potentiostat. The units of this study were calculated as follows: 1) areal loading (mg cm^{-2}) = (total electrode mass (mg) – Al foil mass (mg)) \times active ratio/electrode area (cm^2); 2) compressed density (packing density, mg cc^{-1}) = active loading density (mg cm^{-2})/thickness (cm); 3) total electrode specific capacity (mAh g^{-1}) = capacity (mAh)/total electrode mass (g); and 4) volumetric capacity (mAh cc^{-1}) = capacity (mAh)/active mass (mg) \times compressed density (mg cc^{-1}).

Supporting Information

Supporting Information is available from the Wiley Online Library or from the author.

Acknowledgements

The authors acknowledge Carlos G. Torres Castanedo for helpful discussions on the electrode coating process. This work was primarily supported by the Exelon Corporation. Graphene powder production was supported by the National Science Foundation Scalable Nanomanufacturing Program (NSF CMMI-1727846). Electrochemical characterization was supported by the Center for Electrochemical Energy Science, an Energy Frontier Research Center funded by the U.S. Department of Energy (DOE), Office of Science, Basic Energy Sciences under Award No. DEAC02-06CH1157. This work made use of the EPIC facility of the Northwestern University NUANCE Center, which was supported by the Soft and Hybrid Nanotechnology Experimental (SHyNE) Resource (NSF ECCS-1542205), the Materials Research Science and Engineering Center (NSF DMR-1720139), the State of Illinois, and Northwestern University. Thermogravimetric analysis was performed in the MatCI facility at Northwestern University, which was support by the NSF MRSEC Program (NSF DMR-1720139).

Conflict of Interest

The authors declare no conflict of interest.

Keywords

graphene, high capacity, lithium-ion batteries, Ni-rich cathodes, Pickering emulsions

Received: April 7, 2020
Revised: May 1, 2020
Published online: May 18, 2020

- [1] a) M. Armand, J. M. Tarascon, *Nature* **2008**, 451, 652; b) L. Lu, X. Han, J. Li, J. Hua, M. Ouyang, *J. Power Sources* **2013**, 226, 272.
- [2] a) J. Lee, D. A. Kitchaev, D.-H. Kwon, C.-W. Lee, J. K. Papp, Y.-S. Liu, Z. Lun, R. J. Clément, T. Shi, B. D. McCloskey, J. Guo, M. Balasubramanian, G. Ceder, *Nature* **2018**, 556, 185; b) A. Grimaud, W. T. Hong, Y. Shao-Horn, J. M. Tarascon, *Nat. Mater.* **2016**, 15, 121; c) H. Arai, S. Okada, Y. Sakurai, J.-i. Yamaki, *Solid State Ionics* **1997**, 95, 275.
- [3] V. Etacheri, R. Marom, R. Elazari, G. Salitra, D. Aurbach, *Energy Environ. Sci.* **2011**, 4, 3243.

- [4] a) A. Manthiram, J. C. Knight, S.-T. Myung, S.-M. Oh, Y.-K. Sun, *Adv. Energy Mater.* **2016**, 6, 1501010; b) J. Kim, H. Lee, H. Cha, M. Yoon, M. Park, J. Cho, *Adv. Energy Mater.* **2018**, 8, 1702028.
- [5] J. Lee, A. Urban, X. Li, D. Su, G. Hautier, G. Ceder, *Science* **2014**, 343, 519.
- [6] a) H. Zheng, L. Tan, G. Liu, X. Song, V. S. Battaglia, *J. Power Sources* **2012**, 208, 52; b) M. Ebner, F. Geldmacher, F. Marone, M. Stampanoni, V. Wood, *Adv. Energy Mater.* **2013**, 3, 845.
- [7] L. Jabbour, R. Bongiovanni, D. Chaussy, C. Gerbaldi, D. Beneventi, *Cellulose* **2013**, 20, 1523.
- [8] a) L. Gaines, R. Cuenca, *Costs of Lithium-Ion Batteries for Vehicles*, Argonne National Lab., IL **2000**; b) R. Dominko, M. Gaberscek, J. Drofenik, M. Bele, S. Pejovnik, J. Jamnik, *J. Power Sources* **2003**, 119–121, 770.
- [9] Y. Li, S. Meyer, J. Lim, S. C. Lee, W. E. Gent, S. Marchesini, H. Krishnan, T. Tyliczszak, D. Shapiro, A. L. D. Kilcoyne, W. C. Chueh, *Adv. Mater.* **2015**, 27, 6591.
- [10] a) M. Singh, J. Kaiser, H. Hahn, *J. Electrochem. Soc.* **2015**, 162, A1196; b) B.-S. Lee, Z. Wu, V. Petrova, X. Xing, H.-D. Lim, H. Liu, P. Liu, *J. Electrochem. Soc.* **2018**, 165, A525.
- [11] M. Ender, J. Joos, T. Carraro, E. Ivers-Tiffée, *Electrochem. Commun.* **2011**, 13, 166.
- [12] a) W. Choi, I. Lahiri, R. Seelaboyina, Y. S. Kang, *Crit. Rev. Solid State Mater. Sci.* **2010**, 35, 52; b) M. Yi, Z. Shen, *J. Mater. Chem. A* **2015**, 3, 11700.
- [13] I. H. Son, J. H. Park, S. Park, K. Park, S. Han, J. Shin, S.-G. Doo, Y. Hwang, H. Chang, J. W. Choi, *Nat. Commun.* **2017**, 8, 1561.
- [14] a) G. Kucinskis, G. Bajars, J. Kleperis, *J. Power Sources* **2013**, 240, 66; b) V. Chabot, D. Higgins, A. Yu, X. Xiao, Z. Chen, J. Zhang, *Energy Environ. Sci.* **2014**, 7, 1564.
- [15] a) N. Zhu, W. Liu, M. Xue, Z. Xie, D. Zhao, M. Zhang, J. Chen, T. Cao, *Electrochim. Acta* **2010**, 55, 5813; b) F.-Y. Su, Y.-B. He, B. Li, X.-C. Chen, C.-H. You, W. Wei, W. Lv, Q.-H. Yang, F. Kang, *Nano Energy* **2012**, 1, 429; c) H. Bi, F. Huang, Y. Tang, Z. Liu, T. Lin, J. Chen, W. Zhao, *Electrochim. Acta* **2013**, 88, 414.
- [16] K. Ferchichi, S. Hbaieb, N. Amdouni, V. Pralong, Y. Chevalier, *Ionics* **2014**, 20, 1301.
- [17] M. Li, Y. Zhang, X. Wang, W. Ahn, G. Jiang, K. Feng, G. Lui, Z. Chen, *Adv. Funct. Mater.* **2016**, 26, 8408.
- [18] a) L. A. Belyaeva, P. M. G. van Deursen, K. I. Barbetsea, G. F. Schneider, *Adv. Mater.* **2018**, 30, 1703274; b) Z. Li, Y. Wang, A. Kozbial, G. Shenoy, F. Zhou, R. McGinley, P. Ireland, B. Morganstein, A. Kunkel, S. P. Surwade, L. Li, H. Liu, *Nat. Mater.* **2013**, 12, 925.
- [19] Y. T. Liang, M. C. Hersam, *J. Am. Chem. Soc.* **2010**, 132, 17661.
- [20] a) J. Kim, L. J. Cote, F. Kim, W. Yuan, K. R. Shull, J. Huang, *J. Am. Chem. Soc.* **2010**, 132, 8180; b) J.-W. Kim, D. Lee, H. C. Shum, D. A. Weitz, *Adv. Mater.* **2008**, 20, 3239.
- [21] Y. A. Aggour, *J. Mater. Sci.* **2000**, 35, 1623.
- [22] H. Y. Nan, Z. H. Ni, J. Wang, Z. Zafar, Z. X. Shi, Y. Y. Wang, *J. Raman Spectrosc.* **2013**, 44, 1018.
- [23] E. B. Secor, T. Z. Gao, A. E. Islam, R. Rao, S. G. Wallace, J. Zhu, K. W. Putz, B. Maruyama, M. C. Hersam, *Chem. Mater.* **2017**, 29, 2332.
- [24] X.-Y. Qiu, Q.-C. Zhuang, Q.-Q. Zhang, R. Cao, Y.-H. Qiang, P.-Z. Ying, S.-G. Sun, *J. Electroanal. Chem.* **2013**, 688, 393.
- [25] K. Du, J. Huang, Y. Cao, Z. Peng, G. Hu, *J. Alloys Compd.* **2013**, 574, 377.
- [26] M.-J. Lee, M. Noh, M.-H. Park, M. Jo, H. Kim, H. Nam, J. Cho, *J. Mater. Chem. A* **2015**, 3, 13453.
- [27] S. Sharifi-Asl, F. A. Soto, T. Foroozan, M. Asadi, Y. Yuan, R. Deivanayagam, R. Rojaee, B. Song, X. Bi, K. Amine, J. Lu, A. Salehi-khojin, P. B. Balbuena, R. Shahbazian-Yassar, *Adv. Funct. Mater.* **2019**, 29, 1901110.
- [28] H. Zheng, J. Li, X. Song, G. Liu, V. S. Battaglia, *Electrochim. Acta* **2012**, 71, 258.
- [29] a) M.-H. Liu, C.-W. Jen, J.-M. Chen, S.-C. Liao, *Int. J. Electrochem. Sci.* **2018**, 13, 4350; b) D.-L. Vu, J.-Y. Choi, W.-B. Kim, J. J. Lee, J.-W. Lee, *J. Electrochem. Soc.* **2017**, 164, A2670; c) J. Zheng, W. H. Kan, A. Manthiram, *ACS Appl. Mater. Interfaces* **2015**, 7, 6926.
- [30] L. Jaber-Ansari, K. P. Puntambekar, S. Kim, M. Aykol, L. Luo, J. Wu, B. D. Myers, H. Iddir, J. T. Russell, S. J. Saldaña, R. Kumar, M. M. Thackeray, L. A. Curtiss, V. P. Dravid, C. Wolverton, M. C. Hersam, *Adv. Energy Mater.* **2015**, 5, 1500646.
- [31] S. Yoon, C. W. Lee, Y. S. Bae, I. Hwang, Y.-K. Park, J. H. Song, *Electrochem. Solid-State Lett.* **2009**, 12, A211.
- [32] M. Liang, D. Song, H. Zhang, X. Shi, Q. Wang, L. Zhang, *ACS Appl. Mater. Interfaces* **2017**, 9, 38567.
- [33] D.-L. Vu, J.-w. Lee, *Korean J. Chem. Eng.* **2016**, 33, 514.